RSC Advances



PAPER

View Article Online
View Journal | View Issue



Cite this: RSC Adv., 2025, 15, 27128

Facile preparation of $Fe_3O_4/HAP/Ag$ nanomaterial and photocatalytic degradation of four types of dyes with mechanism[†]

Rui Wu, 10 * Yulin Wang, Junhong Wang, Guanghui Tian, Yapeng Li and Cunfang Liu

The present study involved the facile and green preparation of Fe₃O₄/HAP/Ag (HAP:hydroxyapatite) nanocomposites as catalyst, and followed by comprehensive investigation of their photocatalytic degradation four types of dyes. The photocatalytic degradation of sunset yellow, eosin, allure red and sudan red III dyes under illuminated circumstances were conducted. The structure and morphology of the catalyst was characterized and analyzed by advanced analytical techniques, such as X-ray diffraction (XRD), Fourier transform infrared spectroscopy (FTIR), scanning electron microscopy (SEM), energy dispersive spectroscopy (EDS), mapping and X-ray photoelectron spectroscopy (XPS). The photocatalytic performance of the catalysts were evaluated in detail. The influence of various parameters, including the dosage of catalyst and peroxymonosulfate (PMS) and pH were further examined. The photoelectrochemical studies including cyclic voltammetry (CV), electrochemical impedance spectroscopy (EIS) and diffuse reflectance spectroscopy (DRS), scavenger analysis were discussed. The findings indicated that the Fe₃O₄/HAP/Ag composites demonstrated remarkable capabilities for pollutant removal through photocatalysis, with the degradation rates of 95.6%, 99.5%, 98.4% and 88.6% for sunset yellow, eosin, allure red and sudan red III, respectively. The degradation mechanisms were proposed in detail. The current study provide reference perspective for design of materials for photocatalysis system and wastewater remediation

Received 29th May 2025 Accepted 16th July 2025

DOI: 10.1039/d5ra03777h

rsc.li/rsc-advances

1 Introduction

The rapid development of industrialization has significantly exacerbated environmental pollution issues, particularly due to the extensive application of organic dyes. Varieties of dyes are commercially available, and their broad utilization across sectors like textiles, printing, food processing and cosmetics has rendered them into global environmental contaminants.1 The elevated toxicity, recalcitrant degradability, and propensity for bioaccumulation of these dyes pose significant risks to both ecological systems and human health. Some dyes are not utilized efficiently and are discharged into water environments. This practice not only compromises water quality but also presents direct risks to plant and animal life, as well as human's health via the food chain, thereby increasing the likelihood of cancer.2 Conventional treatment approaches, including physical adsorption, chemical precipitation, and biodegradation, exhibit limitations in efficiency and cost-effectiveness, and they may also lead to secondary pollution. Therefore, it is urgent to

species (ROS) with potent oxidizing capabilities, including hydroxyl radicals ('OH) and superoxide anions (O2'-) generate which indiscriminately degrade organic pollutants.7,8 Photocatalysts, especially semiconductor materials, such as TiO₂, ZnO, GO, BiVO₄ and various other metal oxides, are extensively employed to degrade pollutants. 9,10 Nevertheless, the recovery of the photocatalysts is a big challenge, particularly the small nanoparticle catalyst which hinder the practical implementation. The magnetic Fe₃O₄ or Fe₂O₃ nanoparticles (NPs), addresses this issue effectively and attracted significant interest in photocatalytic processes.11 Although the magnetic Fe₃O₄ NPs enable recycling after treatment, the aggregation is another question in practical applications. Research indicates that encapsulating and loading technology can reduce aggregation in liquid and enhances chemical stability. Hydroxyapatite is a promising material for environmental applications due to its biocompatibility, adsorption property, stability, and substantial surface area. 12,13 The adsorption property of HAP is closely

develop new and efficient degradation technologies to remove

the pollutants and minimize the negative impact on the environment and health.³⁻⁵ Photocatalysis has attracted significant

attention in water treatment due to its environmental friendli-

ness.6 When the catalysts was illuminated, reactive oxygen

Shaanxi Key Laboratory of Catalysis, College of Chemical and Environment Science, Shaanxi University of Technology, Hanzhong, Shaanxi, 723001, China. E-mail: wurui@snut.edu.cn

related to its unique crystal structure and physicochemical

characteristics. HAP belongs to the hexagonal crystal,

[†] Electronic supplementary information (ESI) available. See DOI: https://doi.org/10.1039/d5ra03777h

(A) $\stackrel{\text{pH}=10}{\longleftarrow}$ $\stackrel{\text{pH}=10}{\longleftarrow}$ (B) $\stackrel{\text{pH}=10}{\longleftarrow}$ $\stackrel{\text{pH}=10}{\longleftarrow$

Scheme 1 Synthesis of $Fe_3O_4/HAP/Ag$ composite NPs. (A) The formation of Fe_3O_4 , (B) formation of HAP, (C) formation of $Fe_3O_4/HAP/Ag$.

containing a large number of Ca²⁺, PO₄³⁻ and OH⁻ ions. It easily forms surface unsaturated sites, which can adsorb charged particles through electrostatic interaction or coordination bonds. The hydroxyl of HAP can form hydrogen bonds with polar molecules which facilitate adsorption of polar substances. In addition, HAP NPs have high specific surface area, which promote the adsorption of pollutants. The high specific surface area facilitates the transfer of pollutants to catalyst active sites and enhance light absorption, thereby enhancing photocatalytic efficiency. Furthermore, it was proved that HAP can generate free radicals under UV light irradiation, and the free radicals destructed pollutants which was similar to the function of TiO2.14 However, the application of HAP is limited due to the difficult separation. The heterogeneous HAP/ Fe₃O₄ as composite photocatalyst exhibits nice photodegradation efficacy.

In addition, noble metals, such as Ag, Au, Pt and Pd are excellent catalysts due to surface plasmon resonance (SPR) effect. Deposition of them on the surface of Fe₃O₄/HAP can improve the photocatalytic efficiency. Ag NPs exhibits excellent optical, electrical and thermal properties. Ag NPs act as electron traps to facilitate charge transfer and improve charge separation. 15,16 Specifically, when Ag is deposited onto Fe₃O₄, the magnetic and semiconducting properties of Fe₃O₄ facilitate a magnetic loss effect that promotes the separation of photogenerated electrons from holes. This process enhances both the microwave absorption and photocatalytic properties of the composite material.¹⁷ The incorporation of Fe₃O₄, HAP and noble metals is beneficial to photocatalytic degradation of pollutants with ease of separation, enrichment of target and synergy. As a result, the Fe₃O₄/HAP/Ag composite NPs were employed to photocatalytic degradation of four types of dyes in this work. The synthesis of Fe₃O₄/HAP/Ag composite NPs was shown in Scheme 1.

2 Materials and methods

2.1 Materials

Ferric chloride was purchased from Tianjin Bodi Chemical Co., Ltd. Silver nitrate was purchased from Shaanxi Shenhua Institute of Metallic Materials. Calcium nitrate was purchased from Tianjin Dengfeng Chemical Reagent Factory. Sunset yellow, eosin, allure red and sudan red III were purchased from Tianjin Kemo Chemical Reagent Co. Deionized water was from millipore water purification system and used in all experiments.

2.2 Synthesis of Fe₃O₄/HAP/Ag composite nanomaterials

2.2.1 Synthesis of Fe₃O₄. 2.7140 g ferrous sulfate and 5.413 g ferric chloride were measured and incorporated into deionized water with stir, until fully dissolved. Subsequently, the solution became alkaline by slowly adding sodium hydroxide. Gray green ferrous hydroxide precipitate appeared. Hydrogen peroxide was added dropwise until black precipitate formed. The solution was heated to 60 °C and maintained for 10 min. Subsequently, the precipitate was separated with magnet. The product was wash with deionized water until neutral.

2.2.2 Synthesis of Fe₃**O**₄/**HAP.** The Fe₃O₄/HAP composites were obtained by the co-precipitation method, which simply involved 3.5400 g calcium nitrate and 2.001 g Fe₃O₄ powder in a three-necked flask. The mixture was heated to 100 $^{\circ}$ C using water bath and agitated continuously for 30 minutes. Then, disodium hydrogen phosphate solution containing 3.22 g solute was added dropwise, heated for 2 h. Subsequently, the resultant product was rinsed and dried.¹⁹

2.2.3 Synthesis of Fe₃O₄/HAP/Ag. Ag NPs was obtained following the method. Initially, the mixture of silver nitrate and sodium citrate solution was subjected to magnetic stirring for 10 min. Subsequently, sodium borohydride solution was added with stir for 30 min. Yellow solution appeared, and it was kept at 4 °C for future use. Afterward, 0.1001 g of Fe₃O₄/HAP solid was introduced into 50 mL deionized, then subjected to ultrasonic dispersion for 60 min. The pH was adjusted to approximately 10.0 using sodium hydroxide solution. The Fe₃O₄/HAP solution was heated 70 °C with agitation. 20 mL of the obtained Ag NPs was added to Fe₃O₄/HAP solution at 20-minute intervals, followed 9 times, it then lasted 1 h with stir. Subsequently, the resultant solution was aged for 24 h. The precipitate was washed with deionized water, dried in oven, powdered and stored. The procedure of the procedure of the procedure of the precipitate was washed with deionized water, dried in oven, powdered and stored.

2.3 Characterization and instrumentation

The crystal structures of the $Fe_3O_4/HAP/Ag$ were measured by XRD (D8Advance, Bruker, German). The UV-visible absorption spectra and infrared spectra of the target were identified by using ultraviolet-visible spectrometer (Shimadzu UV-2600, Japan), and infrared spectrometer (Bruker Vertex 70, Switzerland). The structure and morphology of the synthesized $Fe_3O_4/HAP/Ag$ NPs were investigated by transmission electron microscopy and scanning electron microscopy (FEI Tecnai G2 S-Twin, Thermo Fisher, USA). XPS (Kratos, UK) was used to examine the composition of the photocatalyst.

2.4 Photodegradation of organic dyes

Four kinds of organic dyes, including sunset yellow, eosin, allure red and sudan red III were investigated. The obtained

catalyst were introduced into various dye solutions and stirred in dark for 30 min to achieve adsorption–desorption equilibrium. Subsequently, photodegradation was conducted under visible light. At intervals, 2 mL of aliquot were separated by magnet. The UV-visible absorption spectrum of the dyes were measured by UV-vis spectrometer to determine the concentration of dye. Furthermore, the reusability and photochemical performance of the Fe₃O₄/HAP/Ag composite nanomaterials were assessed through four consecutive cycles. The photodegradation rate was calculated using the formula. $R = (C_0 - C/C_0) \times 100\%$, where C_0 is the initial concentration of dye and C is the residual concentration of dye after certain time interval. The influence of various parameters, including the dosage of catalyst, PMS and pH were investigated.

2.5 Exploration of the photodegradation mechanism

The *p*-benzoquinone (BQ), ethylenediaminetetraacetic acid (EDTA), isopropanol (IPA), and methanol (MT) were employed to investigate the photodegradation mechanism. They were used as scavengers of superoxide radicals, holes, hydroxyl radicals, and sulfate radicals, respectively. Follow the previous photodecomposition experimental procedure, different scavengers were introduced into the four types of dyes systems to determine the role of various reactive species.

3 Results and discussion

3.1 Characterization of Fe₃O₄/HAP/Ag composite nanomaterials

3.1.1 XRD analysis. The XRD patterns of the synthesized $Fe_3O_4/HAP/Ag$ composite nanomaterials coincided with the standard patterns of pure Fe_3O_4 , HAP and Ag NPs, as shown in Fig. 1(left). The diffraction peaks at 2θ of 30.1°, 34.2°, 43.8°, 57.2° and 63.3° correspond to the main peaks of pure Fe_3O_4 NPs. The diffraction peak at 31.7° is typical peak of HAP.²³ In addition, the diffraction peaks at 2θ of 38.1°, 44.2°, 64.3° and 77.5° are attributed to the main peaks of Ag NPs.²⁴ Therefore, the XRD results confirmed the formation of the $Fe_3O_4/HAP/Ag$ composite nanomaterials.

3.1.2 IR analysis. The absorption band at 570 cm⁻¹ appeared, which can be attributed to the stretching vibration of the Fe–O bond for Fe₃O₄ in FTIR, as shown in Fig. 1(right). In addition, all the characteristic absorption bands of HAP

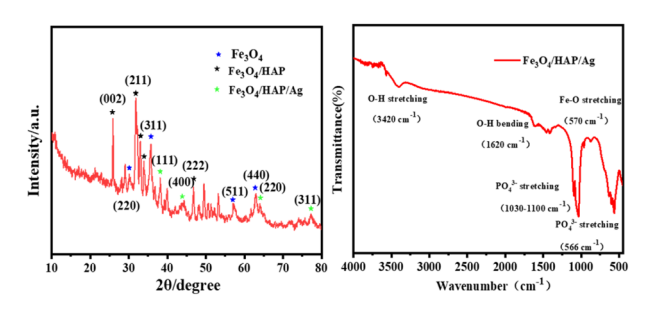


Fig. 1 $\,$ XRD spectrum of Fe $_3O_4/$ HAP/Ag (left), FTIR spectrum of Fe $_3O_4/$ HAP/Ag (right).

appeared in the IR spectra of $Fe_3O_4/HAP/Ag$. Specifically, the stretching vibration of hydroxyl group (O–H) was located at 3420 cm⁻¹, while the bending vibration of O–H appeared at 1620 cm⁻¹. The stretching modes of phosphoric acid (PO_4^{3-}) were observed at 1100 cm⁻¹, 1030 cm⁻¹ and 566 cm⁻¹, respectively.¹¹

3.1.3 XPS analysis. The Fe₃O₄/HAP/Ag composite nanomaterials was further characterized by XPS in Fig. 2. It was clearly confirmed the presence of P, O, Ca, Ag, and Fe elements in Fig. 2(a). XPS witnessed the Ca $2p_{1/2}$ at 349.7 eV and Ca $2p_{3/2}$ at 353.5 eV in Fig. 2(b), which were assigned to the calcium phase in HAp. XPS spectra showed peak at 133 eV for the phosphate group (P 2p) in Fig. 2(c). The fitted peaks at 711 eV (Fe $2p_{3/2}$) and 725 eV (Fe $2p_{1/2}$) showed the high-resolution XPS spectra of Fe in Fig. 2(d), which confirmed the successful synthesis of Fe₃O₄.²⁵ The peak for O 1s was located at 530 eV and it was attributed to the oxygen atom in Fe₃O₄ in Fig. 2(e). Due to the presence of OH and P-O, there were two main peaks for O 1s of XPS spectra, with binding energies at 529 eV and 531.9 eV, respectively.26 The 370.9 eV and 376.9 eV witnessed the XPS of Ag 3d_{5/2} and Ag 3d_{3/2} in Fig. 2(f), respectively.²⁷ According to the analysis of XPS, the results were consistent with Fe₃O₄, HAP and Ag.

3.1.4 SEM, TEM and EDS element mapping analysis. The morphology and structure of $Fe_3O_4/HAP/Ag$ composite nanomaterials were analyzed by SEM and TEM. The SEM of Fe_3O_4/HAP and $Fe_3O_4/HAP/Au$ were shown in Fig. 3(a-c). The HRTEM of $Fe_3O_4/HAP/Ag$ and lattice fringes of HAP were shown

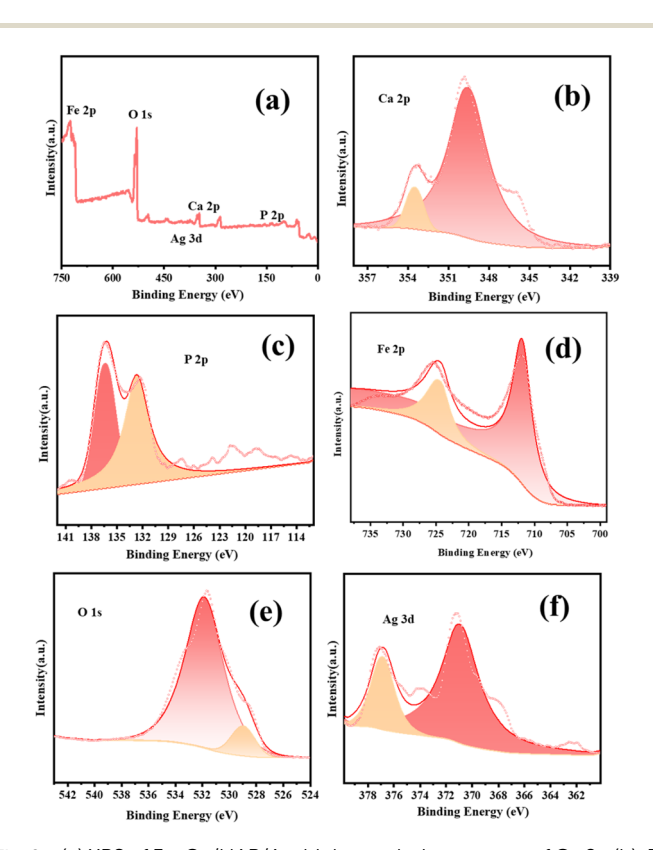


Fig. 2 (a) XPS of Fe $_3$ O $_4$ /HAP/Ag, high-resolution spectra of Ca 2p (b), P 2p (c), Fe 2p (d), O 1s (e) and Ag 3d (f).

in Fig. 3(d) and (e). From SEM, the results showed that the Fe₃O₄ particles was irregular spherical shape with aggregation in Fig. 3(a). As shown in Fig. 3(b), the rod-like deposits were HAP NPs which were loaded on the surface of Fe₃O₄ NPs. When Ag NPs was loaded, Ag NPs were distributed on the surface of Fe₃O₄/HAP, resulting in the formation of Fe₃O₄/HAP/Ag, as shown in Fig. 3(c). The HRTEM image of Fig. 3(d) evidently showed the HAP, Ag and Fe₃O₄. The HAP is regular rod-shape, the length of HAP NPs was more than 50 nm. The Ag NPs were deep black. Fig. 3(e) clearly showed the lattice fringes of HAP. The elemental content of Fe₃O₄/HAP/Ag composite nanomaterials was characterized by EDS, and the EDS mapping of the nanomaterials were shown in Fig. 4(a-f). The results showed that the NPs consisted of the elements of P, O, Ca, Fe, and Ag, which was coincide with XPS, and it was proved the successful synthesis of Fe₃O₄/HAP/Ag. The BET of HAP was provided as ESI (S1).†

3.1.5 Photochemical properties. The optical properties of the composites were assessed by using diffuse reflectance spectroscopy (DRS). The optical bandgap energy (E_g) was calculated from energy-dependent optical absorbance data, which is determined by the Tauc equation: $(\alpha h \nu) 1/n = A(h \nu - \mu) 1/n$ E_{α}). In the equation, α represents the absorption coefficient, ν is the photon frequency, h is Planck's constant (4.14×10^{-15}) eV). A is the proportionality constant, and $E_{\rm g}$ represents the band gap energy. As shown in Fig. 5(a), the $E_{\rm g}$ of Fe₃O₄/HAP/Ag was 1.60 eV, which belong to the narrow band gap material and thus has higher visible light utilization.

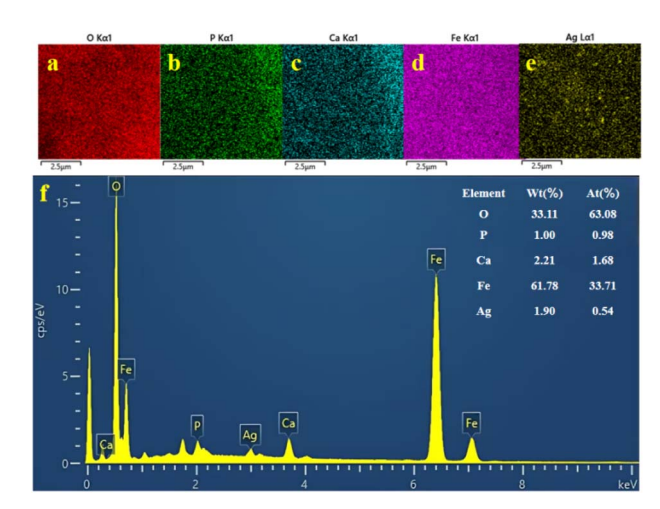


Fig. 4 EDS of Fe₃O₄/HAP/Ag (a) and EDS element mappings of Fe₃O₄/ HAP/Ag (b-f).

In order to investigate the photoelectrochemical properties of Fe₃O₄/HAP/Ag, electrochemical impedance spectroscopy (EIS) and cyclic voltammetry (CV) were carried out. The materials underwent cyclic voltammetry test by using typical threeelectrode system with the potential range of 0.6 to 1.6 V and scan rate of 100 mV s⁻¹. The Fe₃O₄/HAP/Ag showed a satisfactory peak current in Fig. 5(b). It was attributed to its exceptional photocatalytic activity.29 The charge separation efficiency of

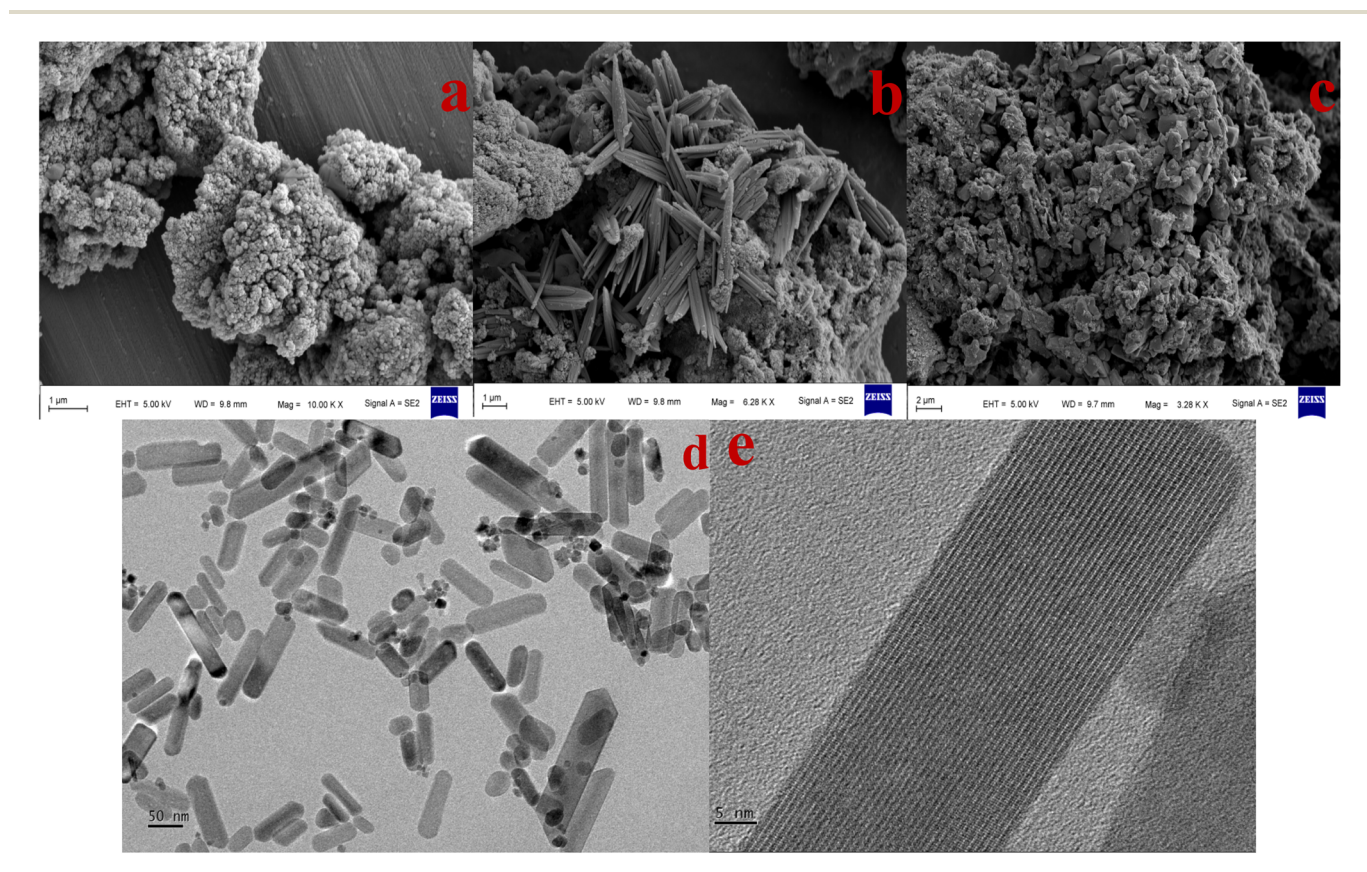


Fig. 3 SEM of Fe_3O_4 (a), SEM of Fe_3O_4 /HAP (b), SEM of Fe_3O_4 /HAP/Ag (c), HRTEM of Fe_3O_4 /HAP/Ag (d), and lattice fringes of HAP (e).

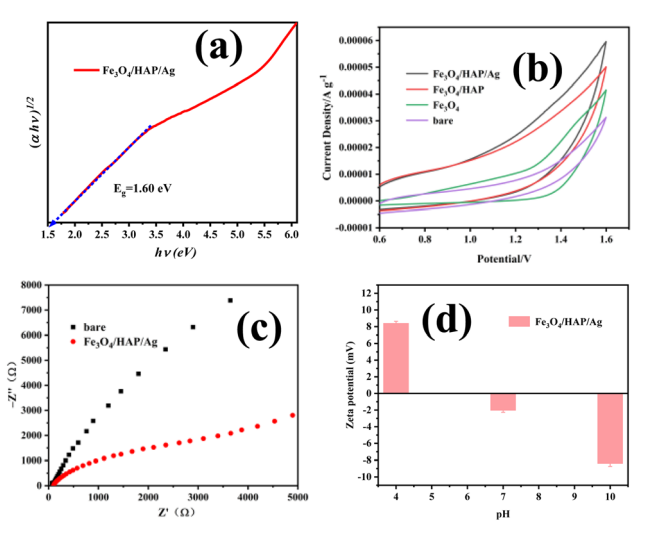


Fig. 5 Band gap of $Fe_3O_4/HAP/Ag$ (a), CV of $Fe_3O_4/HAP/Ag$ (b), EIS of $Fe_3O_4/HAP/Ag$ (c), zeta potential of $Fe_3O_4/HAP/Ag$ (d).

photogenerated electrons and holes are main influencing factor for photocatalysis.

EIS is an effective approach for examining the impact of charge separation. The EIS of bare electrode and ${\rm Fe_3O_4/HAP/Ag}$ were displayed in Fig. 5(c). There was a positive correlation between the arc radius of impedance and the charge transfer resistance of the Nyquist plots, the smaller the arc radius, the higher the charge transfer efficiency. The arc radius of ${\rm Fe_3O_4/HAP/Ag}$ was obviously smaller than that of the bare electrode, which suggested that ${\rm Fe_3O_4/HAP/Ag}$ was capable of accelerating the process of interfacial charge transfer and achieving excellent charge separation and transport.

The zeta potential of Fe $_3$ O $_4$ /HAP/Ag nanocomposites was examined to assess the charge properties and dispersion stability across varying pH. As illustrated in Fig. 5(d), the isoelectric point of Fe $_3$ O $_4$ /HAP/Ag was approximately at 7. It indicated that the zeta potential of the surface closed to zero at this pH, resulting in weak dispersion stability. The surface of Fe $_3$ O $_4$ /HAP/Ag exhibited positive charge under acidic conditions (pH < 7) and negative charge in alkaline conditions (pH > 7). The changes in charge directly influence the adsorption capacity of the material, thus impacting the efficacy of photocatalytic degradation.

3.2 Photocatalytic activity test

The photodegradation was analyzed by monitoring the absorbance peaks at different time intervals according to the concentration of dyes. The photodegradation efficiency was evaluated by the following equation: $R = (C_0 - C/C_0) \times 100\%$, where C_0 and C represent the initial concentration of the dyes and the remaining concentration after a specified time interval, respectively.³¹ In addition, the degradation kinetics was also analyzed. At low concentrations of pollutant, the model is: $\ln(C/C_0) = -kt$, where k is kinetic rate constant, it is calculated by plotting $\ln(C/C_0)$ versus the reaction time.³²

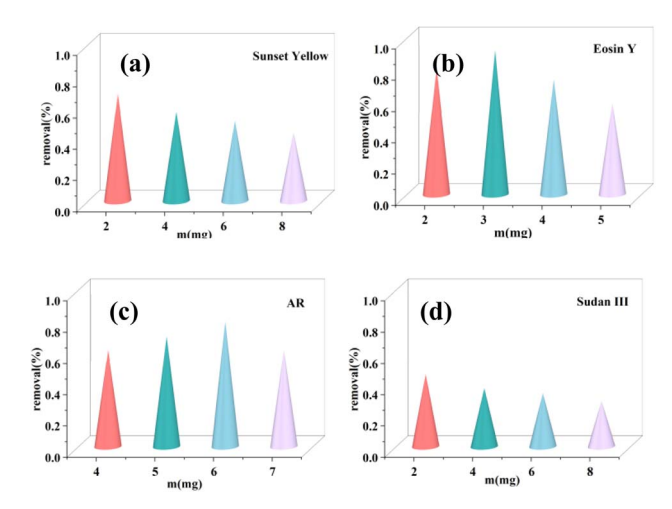


Fig. 6 Effect of catalyst amount on the four types of dyes, (a) sunset yellow, (b) eosin Y, (c) AR and (d) sudan red III.

3.2.1 Optimization of experimental conditions. The photocatalytic degradation of dyes is affected by various operating parameters, including pH, amount of catalyst, initial concentration of dye, and amount of PMS. In view of these parameters played significant role in the photocatalytic degradation of dyes, the effects were discussed in detail.

3.2.1.1 The dose of catalyst. It was pointed out that the amount of catalyst play key role in photocatalytic degradation process.33 Increasing the amount of catalyst can enhance the opportunity for contact between the catalyst and dye molecules. In the early stage of degradation, the generation of 'OH and O2 - radicals were promoted due to the increase of active sites on the surface of the catalyst, which enhanced the degradation efficiency. However, when the concentration of catalyst exceeded a certain value, the turbidity of the solution increased, which would hinder the penetration of UV light and thus affect the photocatalytic efficiency. This study further confirmed the important effect of catalyst dosage on photocatalytic degradation efficiency, as shown in Fig. 6. A decrease in the degradation rate of sunset yellow, eosin, allure red and sudan red III were observed when the amount of catalyst was increased from 2 mg to 8 mg. The highest degradation rates of sunset yellow, allure red and sudan red III were achieved with 2 mg catalyst, and 3 mg for eosin. However, the rate gradually decreased with the increase in dosage. It was demonstrated that high dosage of catalyst may lead to increase in light scattering, which reduces the number of photons received per unit mass of the catalyst, thus decreasing the photocatalytic efficiency. Therefore, the optimal amount of catalyst was important for improving photocatalytic efficiency.

3.2.1.2 The pH of the solution. pH plays a key role in photocatalytic degradation of dye. In order to deeply investigate the effect of pH, different pH values were carried out. The effect of pH on sunset yellow, eosin, allure red and sudan red III were shown in Fig. 7. When the pH was lower than the isoelectric point of the catalyst, the $Fe_3O_4/HAP/Ag$ surface presented positive charge and thus it strongly attracted anions. In acidic

environment, the electrostatic attraction between eosin with negative charge and catalyst with positive charge enhanced.

So, the adsorption capacity of eosin on the surface of Fe₃O₄/HAP/Ag increased and thus enhanced its degradation efficiency.³⁴ In contrast, sunset yellow, allure red and sudan red III showed faster degradation rates under alkaline conditions, which may be attributed to the fact that the photocatalysts are more prone to generate reactive oxygen species, such as hydroxyl radicals, which were essential for photocatalytic degradation of the dyes. Meanwhile, under alkaline conditions, dye molecules may undergo structural changes, resulting ease of adsorption and degradation. Therefore, pH is a crucial parameter in the photocatalytic degradation process.

3.2.1.3 The initial concentration of dyes. It was found that the initial concentration of the dye significantly affected photocatalytic efficiency.35 In our experiments, different initial concentrations of dyes were studied, as shown in Fig. 8. Specifically, the degradation rate of sunset yellow reached 84% after 40 min at 40 mg L⁻¹ with 2 mg catalyst and pH value of 8. The degradation rate reached 82% after 140 min with 30 mg L^{-1} sudan red III under the same conditions. The degradation rate of eosin reached 82% after 35 min with 3 mg catalyst and pH value of 5. Under the conditions of 2 mg of catalyst and pH = 10, the degradation rate of 20 mg L⁻¹ of allure red was 94% after just 10 min. The results suggested that the degradation efficiency showed a decreasing trend with the increase of the initial concentration of the dye. This could be attributed to the fact that the increase in the number of dye molecules led to the occupation of active sites on the surface of catalyst, which hindered the arrival of photons and reduced catalytic efficiency. A moderate initial concentration of dyes facilitate improve the photocatalytic efficiency.

3.2.1.4 The dose of PMS. It was shown that the degradation rate of dyes could be significantly enhanced through the addition of PMS under light conditions.³⁶ The amount of PMS was analyzed in detail. The increase in the initial concentration of PMS will significantly enhanced the photocatalytic efficiency. In

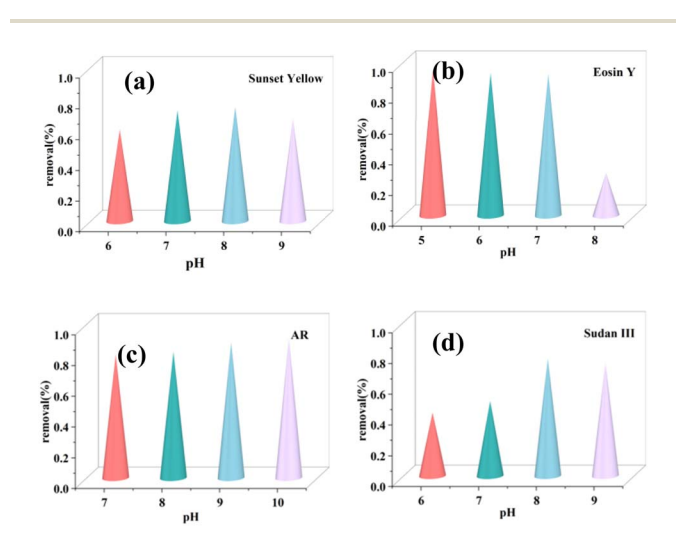


Fig. 7 Effect of pH on the four types of dyes, (a) sunset yellow, (b) eosin Y, (c) AR and (d) sudan red III.

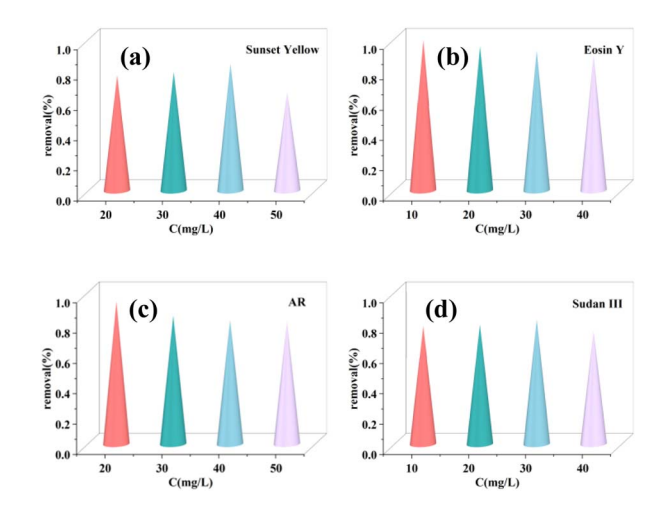


Fig. 8 Effect of initial concentration on the four types of dyes. (a) Sunset yellow, (b) eosin Y, (c) AR and (d) sudan red III.

particular, PMS was able to generate large number of free radicals with strong oxidizing properties under light, which accelerated the degradation of dyes. However, it need to be controlled within appropriate dosage. Because excessive PMS can trigger the quenching free radicals. Therefore, the optimization of the PMS dosage is of significance for improving the photocatalytic degradation efficiency. The effect of PMS on sunset yellow, eosin, allure red and sudan red III were shown in Fig. 9. After careful optimization of the catalyst dosage, pH, initial concentration of dyes, and PMS dosage in the experiment, the best experimental conditions were determined.

Specifically, 40 mg L^{-1} of sunset yellow was degraded under the conditions of 2 mg catalyst, pH = 8 and 4 mg mL⁻¹ PMS for 40 min, and its degradation rate achieved 95.6%. 10 mg L^{-1} of eosin was degraded under the conditions of 3 mg catalyst, pH = 5 and 5 mg mL⁻¹ PMS for 35 min. Its degradation rate achieved 99.5%. 20 mg L^{-1} of allure red achieved 98.4% after 40 min with 2 mg catalyst, 3 mg mL⁻¹ PMS, and pH = $10 \text{ While } 30 \text{ mg L}^{-1}$ of sudan red III achieved 88.6% after 140 min of degradation with 2 mg catalyst, 4 mg mL⁻¹ of PMS, and pH = 8 These results indicated that the photocatalytic degradation efficiency of dyes can be significantly improved by precisely controlling the experimental conditions. Photocatalytic degradation and kinetic simulation curves of sunset yellow, eosin, allure red and sudan red III were shown in Fig. 10(a-h), respectively.

3.2.2 scavenger analyses. In order to deeply reveal the photocatalytic degradation mechanism, the effects of different bursting agents on the photocatalytic degradation reaction were systematically investigated. In the experiments, hydroxyl radicals (OH'), holes (h^+), sulfate radicals and superoxide radicals (O_2 ' $^-$) were targeted and captured by isopropanol (IPA), ethylenediaminetetraacetic acid (EDTA), methyl orange (MT) and benzoquinone (BQ), respectively. The results were shown in Fig. 11. Among the four types of bursting agents, BQ exhibited the most significant inhibition effect. It was indicated that superoxide radicals (O_2 ' $^-$) play key role in the degradation process. Specifically, the added BQ significantly reduced the

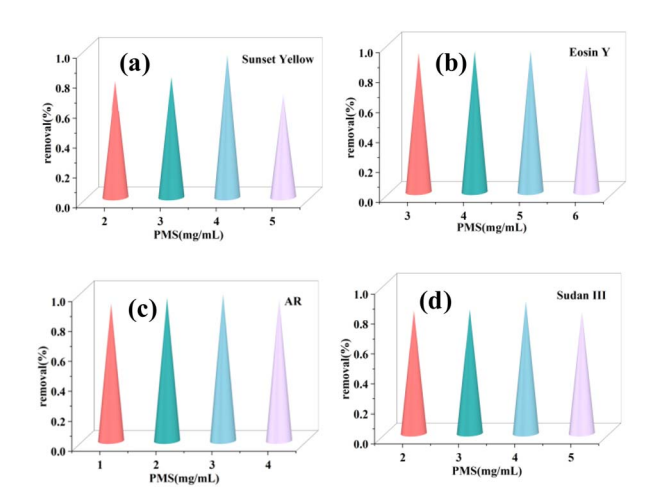


Fig. 9 Effect of the amount of PMS on the four types of dyes (a) sunset yellow, (b) eosin Y, (c) AR and (d) sudan red III.

photodegradation efficiencies of sunset yellow, eosin, allura red, and sudan red III, with degradation rates of 34.2%, 53.7%, 43.6% and 33.6%, respectively. In addition, EDTA, IPA and MT also showed some inhibitory effects. These findings provide important insights into understanding the role of active species in the photocatalytic degradation process.

3.3 Degradation mechanisms

The photocatalytic degradation mechanism was investigated in detail. The mechanism of Fe₃O₄/HAP/Ag nanocomposites in the photocatalytic degradation process involved several key steps, including absorption of light, generation and separation of electron–hole pairs, and generation of reactive oxygen species (ROS). The three layers, namely Fe₃O₄, HAP and Ag play important role in photocatalytic degradation. Each layer of the

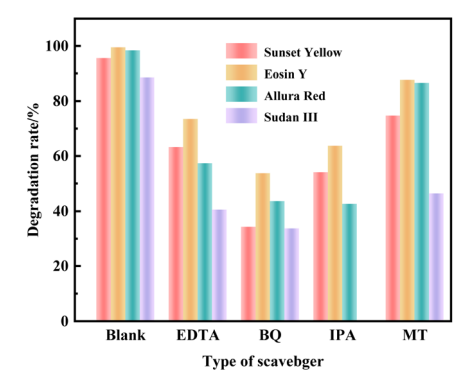


Fig. 11 Photocatalytic degradation of the four types of dye by $Fe_3O_4/HAP/Ag$ with added scavengers.

nanocomposite material has unique role in photocatalytic degradation. Under light radiation condition, the nanocomposites could effectively absorb light, which prompted the electrons to jump from valence band to conduction band, resulting in the generation of photogenerated electron–hole pairs. For Fe₃O₄, it played significant role in separation. As heterogeneous photocatalyst, Fe₃O₄ based nanocomposites showed catalytic activity in some degree due to synergistic effects. ^{14,37,38}

For HAP, the valence band electrons of HAP was excited, they transferred to the conduction band, the holes kept in the valence band under light conditions. The surface of HAP was electrically conductive, associated with change in the PO_4^{3-} , which leaded to the formation of oxygen vacancies. These oxygen vacancies converted to superoxide anions (O_2^{*-}) by adsorbing O_2 and capturing photogenerated electrons from HAP. As a result, the rate of photo-oxidation enhanced. $^{39-41}$ The photogenerated vacancies can directly oxidized the dyes. Meanwhile, hydroxyl radicals ('OH) appeared via H_2O

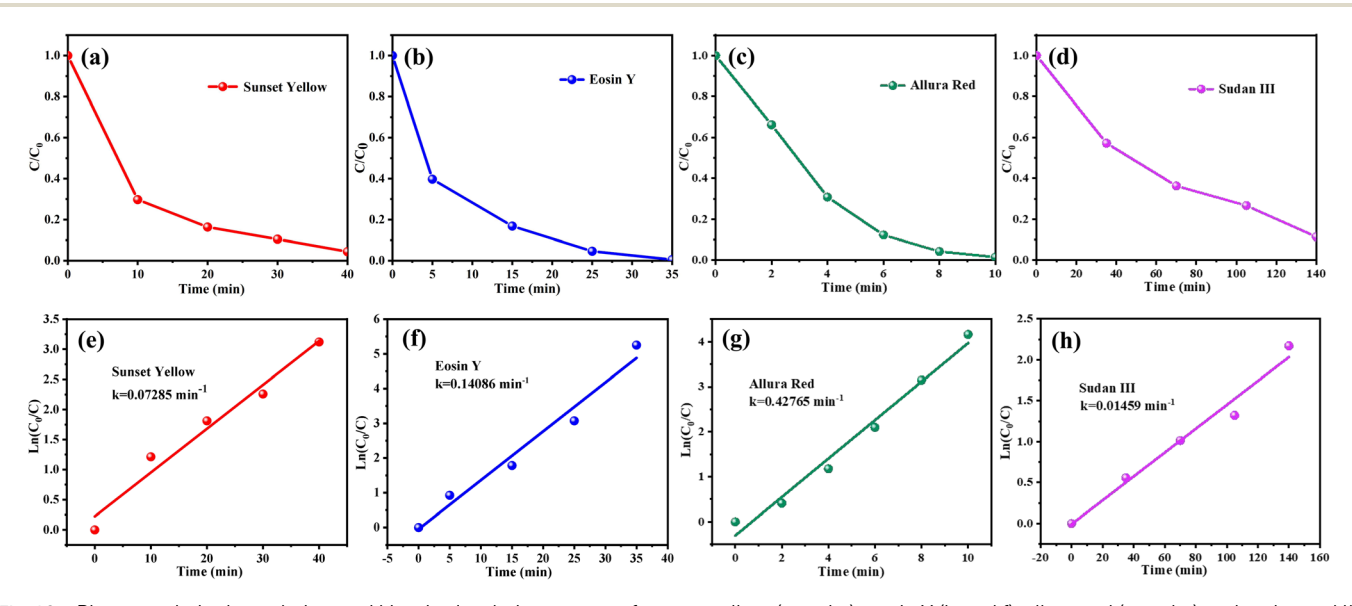


Fig. 10 Photocatalytic degradation and kinetic simulation curves of sunset yellow (a and e), eosin Y (b and f), allure red (c and g) and sudan red III (d and h).

O₂• Fe²⁺
O₂ Fe³⁺ Fe₃O₄
HAP

LSPR

Ag

h⁺ h⁺ h⁺ h

Dye

Fig. 12 Mechanism of photodecomposition of sunset yellow, eosin, allure red and sudan red III by $Fe_3O_4/HAP/Ag$.

molecules and OH- groups as electron donors. So, the formed 'OH and O_2 ' were facile to degrade dyes. The generation of free radical were shown in the equation.

As common precious metal, Ag NPs exhibit strong surface plasmon resonance (SPR) effects, which facilitated absorption of visible lights, and result of hot electrons. The hot electrons from Ag transfer to HAP. While, the holes kept on the surface of Ag. This process can significantly reduced the probability of electron-hole recombination. It also produced localized electromagnetic field enhancement effect, which further promoted the separation of photogenerated electron-hole pairs. 42,43 In addition, because of the combination of HAP and Ag, Schottky barrier formed and promoted charge separation. This Schottky barrier prevented recombination of electrons and holes, thereby prolonged the lifetime of charge carriers. The photoinduced electrons were then captured by O2 and produced O2.-. Furthermore, the holes reacted with H2O molecules and produced 'OH. Meanwhile, 'SO₄" was produced due to the reaction among PMS,O2. and photogenerated electrons. The 'SO₄ interacted with H₂O molecules to generate OH. In one word, these photogenerated electrons and holes react with oxygen and H₂O as well as PMS to produce ROS such as 'OH, O2'-, 'SO4-, and h+, which were capable of non-selectively attacking and degrading the four types of dyes, as shown in Fig. 12. The synergistic effects among the components of Fe_3O_4 , HAP, and Ag in the Fe₃O₄/HAP/Ag nanocomposites collectively contributed to the efficient degradation of dyes.

For Ag:

$$Ag + h\nu \rightarrow Ag^* \rightarrow Ag (e^-) + Ag (h^+)$$

$$Ag (e^-) + HAP \rightarrow HAP (e^-)$$

$$e^- + O_2 \rightarrow {}^{\cdot}O_2^-$$

$$h^+ + OH^- \rightarrow {}^{\cdot}OH$$

$$h^+ + H_2O \rightarrow {}^{\cdot}OH + H^+$$

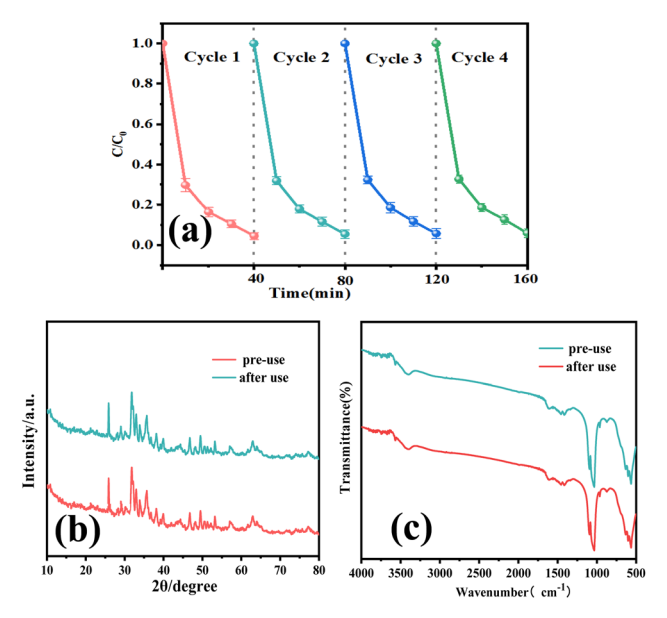


Fig. 13 Recirculation of Fe_3O_4 /HAP/Ag photocatalysts under light (a), XRD (b) and FT- (c) of Fe_3O_4 /HAP/Ag photocatalysts before and after degradation.

For PMS:

$$HSO_5^- + h\nu \rightarrow `SO_4^- + SO_4^{2-} + H^+$$
 $h^+ + HSO_5^- \rightarrow `SO_4^- + H^+$
 $e^- + HSO_5^- \rightarrow `SO_4^- + OH^ `SO_4^- + H_2O \rightarrow `OH + SO_4^{2-} + H^+$
 $`SO_4^- + OH^- \rightarrow `OH + SO_4^{2-}$
 $`SO_4^- + O_2 \rightarrow SO_4^{2-} + `O_2^-$

3.4 Stability and repeatability

In order to comprehensively evaluate the stability and reusability of Fe₃O₄/HAP/Ag photocatalysts in the degradation of dyes, four cycles of experiments were carried out on Fe₃O₄/HAP/Ag under optimal conditions. Despite a minor reduction in the photocatalytic effectiveness of Fe₃O₄/HAP/Ag after each cycle, the elimination rate of sunset yellow remained at 94.2% in the fourth cycle in Fig. 13(a). In addition, the structural stability of Fe₃O₄/ HAP/Ag after photocatalytic degradation was analyzed by FTIR and XRD techniques as shown in Fig. 13(b) and (c). A comparison of the catalyst before and after degradation revealed no significant changes in peak. These results highlighted the excellent structural stability of the photocatalyst. In summary, the synthesized nanocomposite photocatalysts not only exhibited excellent photocatalytic performance but also high structural stability. The Fe₃O₄/HAP/Ag can be considered as highly efficient and stable photocatalyst for the degradation of dyes.

4 Conclusion

In the study, multifunctional three layers of Fe₃O₄/HAP/Ag nanocomposites were successfully prepared and systematically evaluated for their application in photocatalytic degradation of four types of dyes. The experimental results showed that the degradation efficiencies of Fe₃O₄/HAP/Ag photocatalysts for sunset yellow, eosin, allure red and sudan red III reached 95.6%, 99.5%, 99.4% and 88.6%, respectively, under the optimal conditions. In addition, photoelectrochemical properties of the catalyst including cyclic voltammetry (CV), electrochemical impedance spectroscopy (EIS) were studied. It was demonstrated that the Fe₃O₄/HAP/Ag nanocomposites was excellent photocatalyst. The photocatalytic degradation mechanisms was proposed in detail. The 'OH, ${\rm O_2}$ '-, ' ${\rm SO_4}$ -, and ${\rm h}^+$ played significant role in the degradation process. Furthermore, the catalyst exhibited unique stability and reusability. It is candidate for photocatalytic degradation in practical applications. This work not only reveals the potential of Fe₃O₄/HAP/Ag composites as an effective photocatalyst for the removal of hazardous dyes, but also provides new ideas for the development of green and efficient photocatalysts. The Fe₃O₄/HAP/Ag composites not only act as photocatalyst but also candidate as surface-enhanced Raman spectrum substrate and probe in the field of environment, food, biology, medicine.

Data availability

All data supporting the findings of this study are included in the published article and its ESI files.†

Author contributions

Rui Wu: conceptualization, supervision, investigation, methodology, writing – review & editing, funding acquisition. Yulin Wang: writing – original draft, investigation. Junhong Wang, review. Guanghui Tian, Yapeng Li and Cunfang Liu: formal analysis.

Conflicts of interest

The authors declare no conflict of interest.

Acknowledgements

This work was financially supported by Key Research and Development Plan of Shaanxi Province (2024GX-YBXM-318), Qinchuangyuan Project (2024PT-ZCK-38), Shaanxi Provincial Natural Science Basic Research Plan General Project (2025JC-YBMS-146). The Brinstorm project on Social Development by the Department of Science and Technology of Shaanxi Province (2025SF-YBXM-475). National Natural Science Foundation of China (22177066).

References

- 1 A. Tkaczyk, K. Mitrowska and A. Posyniak, Synthetic organic dyes as contaminants of the aquatic environment and their implications for ecosystems: a review, *Sci. Total Environ.*, 2020, 717, 13722–13778.
- 2 T. A. Aragaw, A review on biodegradation of textile dye wastewater: challenges due to wastewater characteristics and the potential of alkaliphiles, *J. Hazard. Mater. Adv.*, 2024, **16**, 100493–100513.
- 3 F. Y. Jin, J. X. Lu, F. Sun, F. Yang and Z. H. Li, Application and development of sludge-based materials for environmental pollution remediation: a bibliometric review from 2004 to 2024, *RSC Adv.*, 2025, **15**, 8072–8087.
- 4 J. Uddin, R. Abdur, M. R. Hossain, S. Aziz, M. S. Jamal, M. A. A. Shaikh and M. Hossain, Phase tunable nickel doped Mn₃O₄ nanoparticle synthesis by chemical precipitation: kinetic study on dye degradation, *Nanoscale Adv.*, 2024, **6**, 902–909.
- 5 M. Shabir, M. Yasin, M. Hussain, I. Shafiq, P. Akhter, A. S. Nizami and Y. K. Park, A review on recent advances in the treatment of dye-polluted wastewater, *J. Ind. Eng. Chem.*, 2022, 1, 112–121.
- 6 S. Shahzadi, S. Fatima, Q. Ain, Z. Shafiq and M. R. S. A. Janjua, A review on green synthesis of silver nanoparticles (SNPs) using plant extracts: a multifaceted approach in photocatalysis, environmental remediation, and biomedicine, *RSC Adv.*, 2025, **15**, 3858–3903.
- 7 S. M. Shabil, H. Anwar and F. N. Musthafa, Photocatalytic degradation of organic dyes using reduced graphene oxide (rGO), *Sci. Rep.*, 2024, **14**, 3608–3622.
- 8 C. C. Rafael, N. M. J. Ricardo and M. P. Saraiva, Fluorometric kinetic determination of aflatoxin B1 by combining Cd-free ternary quantum dots induced photocatalysis and chemometrics, *Microchem. J.*, 2023, **85**, 108300–108306.
- 9 S. Alwera, V. S. Talismanov, V. Alwera and D. Domyati, *Biointerface Res.* Synthesis and characterization of Sndoped CeO₂-Fe₂O₃ nanocomposite and application in photocatalytic degradation of Sudan I, *Appl. Chem.*, 2023, 13, 179–193.
- 10 M. Liu, Y. Ye, J. Ye, T. Gao, D. Wang, G. Chen and Z. Song, Recent advances of magnetite (Fe₃O₄)-based magnetic materials in catalytic applications, *Magnetochemistry*, 2023, 9, 110–142.
- 11 X. X. Li, H. W. Zhou, R. R. Qian, X. Zhang and L. Yu, A concise synthesis of Se/Fematerials for catalytic oxidation reactions of anthracene and polyene, *Chin. Chem. Lett.*, 2025, 36, 110036–110039.
- 12 J. Kalita, L. Bharali and S. S Dhar, Zn supported on hydroxyapatite encapsulated Fe₃O₄ (Fe₃O₄/HAp@Zn) nanocomposite for visible light driven photodegradation of ciprofloxacin antibiotics, *Interactions*, 2024, **245**, 313–332.
- 13 A. Biedrzycka, A. G. Płaska and E. Skwarek, Study of the effect of uranium recovery at Hap/Fe₂O₃ composite and Fe₂O₃ interfaces on the parameters of the electrical double layer, J. Mater. Chem. A, 2023, 11, 24281–24298.

14 M. Golshan, M. Zare, G. Goudarzi, M. Abtahi and A. A. Babaei, Fe₃O₄@HAP-enhanced photocatalytic degradation of Acid Red73 in aqueous suspension: optimization, kinetic, and mechanism studies, *Mater. Res.* Bull., 2017, 91, 59–67.

- 15 R. C. Suciu, M. Zagrai, A. Popa, D. Toloman, C. Berghian-Grosan, C. Tudoran and M. Stefan, The influence of Ag⁺/Ti⁴⁺ ratio on structural, optical and photocatalytic properties of MWCNT-TiO₂-Ag nanocomposites, *Inorganics*, 2023, **11**, 249–268.
- 16 Y. Liu, C. H. Liu, T. Debnath, Y. Wang, D. Pohl, L. V. Besteiro and D. Ma, Silver nanoparticle enhanced metal-organic matrix with interface-engineering for efficient photocatalytic hydrogen evolution, *Nat. Commun.*, 2023, 14, 541–553
- 17 X. Meng, Y. Peng, Z. Shao, X. Huang, H. Wei, Z. Wei and S. Zhao, Controllable construction of hollow Fe₃O₄/Ag particles for microwave absorption and photocatalysis, *Chem. Eng. J.*, 2024, **492**, 152282–152293.
- 18 C. Luo, Y. Hu, S. Xing, W. Xie, C. Li, L. He and X. Zeng, Adsorption-precipitation-cross-linking immobilization of GDSL-type esterase from Aspergillus niger GZUF36 by polydopamine-modified magnetic clarity tetroxide nanocouplings and its enzymatic characterization, *Int. J. Biol. Markers*, 2023, 245, 125533–125544.
- 19 A. Biedrzycka, E. Skwarek, D. Osypiuk and B. Cristóvao, Synthesis of hydroxyapatite/iron oxide composite and comparison of selected structural, surface, and electrochemical properties, *Materials*, 2022, 15, 1139–1157.
- 20 R. Wu, X. Song, Y. L. Wang and Q. Zhang, Detection of pesticide residue using an $Fe_3O_4/GO/Ag$ nanocomposite as a SERS substrate and mechanism investigation, *RSC Adv.*, 2025, **15**, 10310–10318.
- 21 Y. F. Chen, W. R. Chang, J. H. Wang, C. F. J. Kuo, C. C. Cheng and C. W. Chiu, Triangular silver nanoplates/graphene oxide nanohybrids on flexible substrates for detection of bacteria via surface-enhanced Raman spectroscopy, *ACS Appl. Nano Mater.*, 2023, **6**, 13604–13615.
- 22 Y. Li, Z. Lai, Z. Huang, H. Wang, C. Zhao, G. Ruan and F. Du, Fabrication of BiOBr/MoS₂/graphene oxide composites for efficient adsorption and photocatalytic removal of tetracycline antibiotics, *Appl. Surf. Sci.*, 2021, **550**, 149342–149352.
- 23 S. Valizadeh, M. H. Rasoulifard and M. S. S. Dorraji, Modified Fe₃O₄-hydroxyapatite nanocomposites as heterogeneous catalysts in three UV, Vis and Fenton like degradation systems, *Appl. Surf. Sci.*, 2014, **319**, 358–366.
- 24 A. T. Mosleh, E. A. Kamoun, S. H. El-Moslamy, S. A. Salim, H. Y. Zahran, S. H. Zyoud and I. S. Yahia, Performance of Ag-doped CuO nanoparticles for photocatalytic activity applications: synthesis, characterization, and antimicrobial activity, *Discover Nano*, 2024, 19, 166–187.
- 25 H. Kohzadi and M. Soleiman-Beigi, XPS and structural studies of Fe₃O₄-PTMS-NAS@Cu as a novel magnetic natural asphalt base network and recoverable nanocatalyst for the synthesis of biaryl compounds, *Sci. Rep.*, 2021, 11, 24508–24522.

- 26 G. Bharath, A. Naldoni, K. H. Ramsait, A. Abdel-Wahab, R. Madhu, E. Alsharaeh and N. Ponpandian, Enhanced electrocatalytic activity of gold nanoparticles on hydroxyapatite nanorods for sensitive hydrazine sensors, *J. Mater. Chem. A*, 2016, **4**, 6385–6394.
- 27 P. Prieto, V. Nistor, K. Nouneh, M. Oyama, M. Abd-Lefdil and R. Díaz, XPS study of silver, nickel and bimetallic silvernickel nanoparticles prepared by seed-mediated growth, *Appl. Surf. Sci.*, 2012, 258, 8807–8813.
- 28 P. R. Jubu, F. K. Yam, V. M. Igba and K. P. Beh, Tauc-plot scale and extrapolation effect on bandgap estimation from UV-vis-NIR data a case study of β-Ga₂O₃, *J. Solid State Chem.*, 2020, **290**, 121576–121606.
- 29 N. A. Arzaee, M. F. M. Noh, A. Ab. Halim, M. A. F. A. Rahim, N. S. H. M. Ita, N. A. Mohamed and M. A. M Teridi, Cyclic voltammetry a promising approach towards improving photoelectrochemical activity of hematite, *J. Alloys Compd.*, 2021, 852, 156757–156765.
- 30 A. Zulkiflee, M. M. Khan, M. Y. Khan, A. Khan, A. C. Ummer and M. H. Harunsani, Zirconium-doped BiOCl for enhanced visible light-induced photocatalytic degradation of RhB dye and photoelectrochemical studies, *New J. Chem.*, 2023, 47, 16577–16585.
- 31 I. Abdelfattah and A. M. El-Shamy, A comparative study for optimizing photocatalytic activity of TiO₂-based composites with ZrO₂, ZnO, Ta₂O₅, SnO, Fe₂O₃, and CuO additives, *Sci. Rep.*, 2024, **14**, 27175–27201.
- 32 Ö. Tuna, H. H. Mert, M. S. Mert and E. B. Simsek, Tailoring the surface features of CaWO₄ by coupling with tubular g-C₃N₄ for enhanced solar photocatalysis and thermal energy storage, *J. Energy Storage*, 2024, **86**, 111398–111413.
- 33 G. Singh, M. K. Ubhi, K. Jeet, C. Singla and M. Kaur, A review on impacting parameters for photocatalytic degradation of organic effluents by ferrites and their nanocomposites, *Processes*, 2023, **11**, 1727–1750.
- 34 T. T. Nguyen, S. N. Nam, J. Son and J. Oh, Tungsten trioxide (WO₃)-assisted photocatalytic degradation of amoxicillin by simulated solar irradiation, *Sci. Rep.*, 2019, **9**, 9349–9367.
- 35 S. Arabian, A. Gordanshekan, M. Farhadian, A. R. S. Nazar, S. Tangestaninejad and H. Sabzyan, Adsorption/photocatalytic degradation of Cefixime by the green Bi₂WO₆/g-C₃N₄/ZIF-67 dual S-scheme heterojunction: artificial neural network, genetic algorithm, density functional theory, and toxicity assessments, *Chem. Eng. J.*, 2024, 488, 150686–150707.
- 36 B. Pan, W. Chen, L. Zhou, X. Lai, J. Qin and C. Wang, CoFe₂O₄/carbon nitride Z-scheme heterojunction photocatalytic PMS activation for efficient tetracycline degradation: accelerated electron transfer, *Process Saf. Environ.*, 2024, **191**, 2522–2532.
- 37 A. Anjali, B. Gupta, M. Tripathi, K. Sahni, N. Sharma and S. Pandit, Enhancing photocatalytic performance of Fe₃O₄ nanoparticles and Fe₃O₄@ZnO nanocomposites, *Ionics*, 2024, **30**, 1–13.
- 38 A. Shojaie, M. Fattahi, S. Jorfi and B. Ghasemi, Synthesis and evaluations of Fe₃O₄-TiO₂-Ag nanocomposites for photocatalytic degradation of 4-chlorophenol (4-CP): effect

- of Ag and Fe compositions, Int. J. Ind. Chem., 2018, 9, 141-151.
- 39 S. Chidambaram, B. Pari, N. Kasi and S. Muthusamy, ZnO/Ag heterostructures embedded in Fe₃O₄ nanoparticles for magnetically recoverable photocatalysis, *J. Alloys Compd.*, 2016, 665, 404–410.
- 40 J. S. Wu, J. Lu, X. Ji, G. Tian and F. Zhang, Constructions of Fe₃O₄/HAp/Au nanohybrids with multifunctional structure for efficient photocatalysis and environmental remediation of organic dyes, *J. Mol. Struct.*, 2023, **1278**, 134908–134914.
- 41 R. X. Wang, Y. J. Wang, J. Y. Chen, Y. Yin, N. N. Zheng, M. D. Li, S. Zhao, X. Han, Q. W. Li, Y. M. Niu, L. Zhang and S. Pan, Photocatalytic TiO₂/HAP nanocomposite for

- antimicrobial treatment, promineralization, and tooth whitening, *RSC Adv.*, 2025, **15**, 13453–13467.
- 42 A. Kumar, S. K. Sharma, G. Sharma, A. A. H. Al-Muhtaseb, M. Naushad, A. A. Ghfar Kumar, A. Sharma, S. K. Sharma, G. Al-Muhtaseb, A. A. H. Naushad, M. Ghfar, A. A. Stadler and F. J. Stadler, Wide spectral degradation of Norfloxacin by Ag@BiPO₄/BiOBr/BiFeO₃ nano-assembly: elucidating the photocatalytic mechanism under different light sources, *J. Hazard. Mater.*, 2019, 364, 429–440.
- 43 S. Q. Zhang, T. Yu, H. Wen, R. Guo, J. J. Xu, R. X. Zhong, X. Li and J. H. You, Enhanced photocatalytic activity of a visible-light-driven ternary WO₃/Ag/Ag₃PO₄ heterojunction: a discussion on electron transfer mechanisms, *RSC Adv.*, 2020, **10**, 16892–16903.